Reports in Mechanical Engineering
Vol. 7, No. 1, 2026, pp. 105-117
ISSN: 2683-5894, DOI: https://doi.org/10.31181/rme530

Optimisation of a Dual Cylindrical Cam Mechanism for Energy Storage and Torque Efficiency

Matteo Monfrini*, Roberto Pagani, Alberto Borboni
Department of Mechanical and Industrial Engineering, University of Brescia, Via Branze 38, Brescia, 25123, BS, Italy

Article Info

Article history:

Received January 4, 2026
Revised February 7, 2026
Accepted February 20, 2026

Keywords:

Cam,
Cylindrical Cams,
Energy Storage,
Optimisation,
Dual Cam with a Shared Follower

ABSTRACT

This paper presents a novel concentric dual-cylindrical cam mechanism designed to store energy in a spring and deliver a specified torque at precise angular positions. Two coaxial cylindrical cams act on a single spring-loaded follower, enabling energy absorption during one phase of motion and release during another. A kinetostatic theoretical model is developed to describe the system behaviour, providing equations for internal forces and output torque in both compression and release phases. By analysing a dimensionless efficiency metric (released-to-input torque) and exploring the design space, an optimal cam inclination for both cams is identified that maximises torque efficiency. Under the model assumptions, this optimum is independent of friction coefficient and external load. An experimental program on prototype cam pairs validates the model: measured torque–angle characteristics agree strongly with predictions for both tested designs. The findings demonstrate improved torque delivery and broad applicability to compact energy-storage systems that require controlled torque profiles and high energy efficiency, including robotic actuators, prosthetic limbs, and automotive mechanisms.

Corresponding Author:

Matteo Monfrini
Department of Mechanical and Industrial Engineering, University of Brescia, Via Branze 38, Brescia, 25123, BS, Italy
Email: monfrini.matteo@gmail.com

1. Introduction

Solar-powered long-endurance UAVs, Cam mechanisms are critical components in many mechanical applications, valued for converting rotary motion into precise linear or oscillatory movements. Their use spans automotive, automation, and robotics, where accurate motion control is essential. This work (Hren et al., 2018) offers an approach to future torque-shaping methods for this configuration. Cylindrical cam mechanisms, in particular, are appreciated for compactness and for enabling com plex follower paths in space-constrained environments (Mundo et al., 2006). Achieving optimal performance, especially efficiency and targeted torque output, requires careful analysis of design parameters such as cam inclination and energy management strategies, as shown in studies on cam optimisation and torque transmission efficiency. This study introduces a novel cylindrical cam mechanism designed to deliver a specified torque at a precise follower angular position relative to two interacting cams. The system departs from conventional solutions by using a spring-based energy-absorption and release process. Rather than prioritizing continuous motion, the design exploits spring compression and expansion to store and release energy at selected points in the cycle. Prior studies have explored spring-follower cam systems for torque control; however, no previous work has examined a concentric dual-cam mechanism with a spring for torque shaping, nor the effect of cam inclination on efficiency (Aversa et al., 2017). Our research identifies the optimal cam inclination angles to maximize mechanism efficiency. Using modeling and static equilibrium analysis, we derive expressions for the compressing and stretching torque phases and evaluate the resulting efficiency. Results show that efficiency peaks at a specific inclination angle, independent of friction coefficients or external loads. This indicates that adjusting cam angle alone can optimize performance in torque intensive applications.

2. Literature Review

Cam mechanisms are foundational in mechanical systems requiring precise motion control. The drive toward compact, energy-efficient actuation has renewed interest in optimizing cam profiles, torque generation and energy management, particularly in systems incorporating springs for energy storage.

Several studies have addressed torque optimisation through cam profile design. Gao et al. (Gao et al., 2018) proposed a method for generating cam profiles that achieve predefined torque outputs in spring-cam systems, highlighting the strong dependency of torque behavior on geometric parameters. Demeulenaere and De Schutter (Demeulenaere & De Schutter, 2005) introduced an inverted cam mechanism designed for torque balancing using spring compensation, thereby enhancing input energy efficiency.

Spring-based energy return systems have been investigated in both robotics and prosthetics. Sun et al. (Sun et al., 2019) designed a prosthetic actuator utilizing conjugate cylindrical cams and dual springs to achieve nonlinear torque characteristics and energy recovery. Kim et al. (Kim et al., 2020) proposed a compact actuator using dual cylindrical cams to mitigate gravitational torque, demonstrating improved energy reuse and mechanical simplicity.

In tribological contexts, friction and wear significantly impact cam system performance. Cardoso et al. (Cardoso et al., 2025) demonstrated the role of lubricant properties in shaping torque responses under preload conditions, while Baş (Baş, 2021) emphasized the importance of material selection and surface preparation in reducing wear.

Cylindrical cam systems, particularly those with conjugate profiles, provide robust torque control in confined volumes. Tsay et al. (Tsay et al., 2002) developed torque-balancing cams for globoidal indexing mechanisms, optimizing output stability under varying loads. Català et al. (Català et al., 2016) addressed failure prevention in conjugate cams through strategic geometry and stress distribution.

Angeles and López-Cajún (Angeles & López-Cajún, 2012) proposed a generalized optimisation frame work for cam mechanisms, using analytical and numerical tools to synthesize cam profiles under multiple performance constraints. Their work supports automated design tailored to specific force or displacement objectives.

Finally, friction losses may be reduced by adopting a follower equipped with rollers, transforming sliding contact into rolling contact. In addition, extensive tribological studies on cam-follower systems provide guidelines for surface treatments, lubrication regimes, and material selection to mitigate wear and improve efficiency (Alakhramsing et al., 2018; Alamsyah et al., 1989; Cerit et al., 2023; Kolozsvary, 1973).

Despite advances in the field, no prior studies have examined the combined effects of dual concentric cylindrical cams, spring–follower interaction, and torque shaping in a compact configuration. The mechanism explored in this study fills this gap by introducing a spring-loaded follower driven by dual cams with tunable inclination angles, enabling friction-independent torque control and experimentally verified performance.

3. Mechanism Model

The mechanism consists of two cylindrical elements with an effective radius r. The first cylinder is fixed, whereas the second rotates along the $z-axis$ by an angle θ under the action of an external torque $T_C(\theta)$. Both cylinders feature a helical groove, defined by Eq. (8), machined to form two concentric cylindrical cams: cam_1 (outer) and cam_2 (inner). A cylindrical follower is rigidly connected to a carriage. It is constrained to undergo combined rotation and translation along the *z*-axis, engaging both helical grooves. Each cam is machined symmetrically to avoid a net overturning moment on the follower; consequently, the cylinder provides two identical actions, one on each side. For simplicity, only one side is considered in the following analysis.

$$\begin{cases} x_i(\psi_i) = r_i \cos(\psi_i) \\ y_i(\psi_i) = r_i \sin(\psi_i) \text{ with } \psi_i \in [0,2\pi]. \\ z_i(\psi_i) = g_i(\psi_i) \end{cases} \quad (1)$$

The mathematical model is developed under a quasi-static assumption, i.e., the motion is sufficiently slow that inertial effects can be neglected; accordingly, force equilibrium and power balance are enforced instantaneously. This assumption is justified by the spring's high rigidity and the system's lightness, which result in a high natural frequency relative to the angular acceleration, thereby making the inertial forces negligible (Tsay et al., 2002). At higher operating speeds, however, the system dynamics could introduce significant inertial effects. These could impact the accuracy of the torque profiles and energy efficiency by causing delays in force transmission and potential vibrations. If such dynamic effects become prominent, a more detailed dynamic analysis, including consideration of inertial forces and damping, would be required. The function g sub i. describes the helical grooveis described by the function $g_i(\psi_i)$, which defines the generic pitch law of the helix and the corresponding lead angle λ_i, measured with respect to the horizontal plane (acute angle). In particular, with $z = g_i(\psi_i)$, the local lead angle satisfies $tan\lambda_i(\psi_i) = g_i'(\psi_i)/\, r_i$.

Coulomb friction is assumed at all contact interfaces; the friction coefficients between the follower and cam_1 (outer cam) and cam_2 (inner cam) are denoted by μ_1 and μ_2, respectively. The associated friction angles are introduced as$i$ $\phi_i = arctan(\mu_i)$, with $i \in \{1,2\}$. The total axial force $F_{z,\text{tot}}$ that the mechanism must balance comprises three contributions. First, a possibly nonlinear spring exerts a position-dependent force $F_s(z)$, defined as $F_s(z) = F_0 + \int k(\xi)\mathrm{d}\xi$, where F_0 is the preload and k is the local stiffness; the variable z describes the follower axial displacement and the corresponding spring compression. In addition, a piston rigidly attached to the follower translates along the z axis in an oil bath, introducing a damping force $D(\dot{z})$ that opposes the motion. A general damping law with distinct parameters for the upstroke and downstroke is adopted, namely $D(\dot{z}) = \frac{1+\mathrm{sgn}(\dot{z})}{2} c\dot{z} + \frac{1-\mathrm{sgn}(\dot{z})}{2} q|\dot{z}|\dot{z}$, where the linear term $c\dot{z}$ models viscous (laminar) effects and the quadratic term $q|\dot{z}|\dot{z}$ models localized (turbulent) pressure losses. The resulting kinetostatic formulation relates the input rotation-start equation theta to the output translation-start θ to the output translation z. Let γ denote the relative angle between cam_1 and the cylinder, and let ϕ denote the relative angle between cam_2 and the cylinder; the input rotation satisfies $\theta = \phi + \gamma$. The geometry of cam_1 implies that the axial dis. In contrast,t z_1 is a function of the cam parameter ψ_1, according to $\mathrm{d}z_1/\mathrm{d}\psi_1 = r\tan\left(\lambda_1(\psi_1)\right)$, while cam $_2$ imposes $\mathrm{d}z_2/\mathrm{d}\psi_2 = r\tan\left(\lambda_2(\psi_2)\right)$. At any admissible configuration, compatibility requires $z = z_1 = z_2$, so that z is used as the common axial coordinate for the entire mechanism. For convenience, the kinematics of the second cam are expressed through the functional relationship $\phi = \phi_s(z)$, which yields $\dot{\phi} = \phi_s'(z)\dot{z}$. Using $\gamma = (\theta - \phi)$ hence $\dot{\psi}_1 = \dot{\gamma} = (\dot{\theta} - \dot{\phi})$, the axial velocity $\dot{z} = v_z$ can be written as $\dot{z} = \frac{\mathrm{d}z}{\mathrm{d}\psi_1}\dot{\psi}_1 = r\tan\left(\lambda_1(\psi_1)\right)(\dot{\theta} - \dot{\phi}) = r\tan\left(\lambda_1(\psi_1)\right)\left(\dot{\theta} - \phi_s'(z)\dot{z}\right)$. Solving for $\dot{z}$ in terms of $\dot{\theta}$ yields the instantaneous kinematic transmission Eq. (9).

$$v_z = \dot{z} = \frac{dz}{d\theta}\dot{\theta} = \frac{r\tan\left(\lambda_1(\psi_1)\right)}{1+r\tan\left(\lambda_1(\psi_1)\right)\phi_s'(z)}\dot{\theta} \tag{2}$$

This relationship is fundamental but exhibits a potential kinematic singularity if the denominator vanishes $(1 + r\tan\left(\lambda_1(\psi_1)\right)\phi_s'(z) = 0)$, a condition corresponding to mechanism jamming or binding, which must be avoided during the design phase. To determine the required torque $T_c(\theta)$The equilibrium of forces acting on the pin is maintained at every instant. It is useful to resolve the forces into the local coordinate directions of the system. Slot inclination: The local inclination of the cam $_2$ is $\lambda_2(\psi_2)$, or also defined by $\tan\left(\lambda_2(\phi_2)\right) = r\phi_s'(z)$. The total resistive force along the z-axis is $F_{z,\text{tot}}(z,\dot{z}) = F_s(z) + F_{\text{ext}}(z) + D_v(z,\dot{z})$. Considering the contact between cam c_1 and the follower, the presence of friction μ_1 modifies the effective thrust angle, resulting in a circumferential component $F_\theta^{cam_1}$ and an axial component $F_z^{\text{cam}\,1}$, whose ratio is $\left|F_\theta^{\text{cam}\,1}\right| / \left|F_z^{\text{cam}\,1}\right| = \tan\left(\lambda_{\text{eff}\,1}\right)$, where the effective angle $\lambda_{\text{eff}\,1} = \lambda_1(\psi_1) + \mathrm{sgn}(\dot{z})\phi_1$. Similarly, for the contact between cam and the follower, we define the effective angle $\lambda_{\text{eff}\,2} = \lambda_2(\psi_2) + \mathrm{sgn}(\dot{z})\phi_2$. The local static equilibrium of the pin requires, circumferential equilibrium: $F_\theta^{\text{cam}_1} + F_\theta^{\text{cam}_2} = 0$, and axial equilibrium: $F_z^{\text{cam}_2} + F_z^{\text{cam}_1} - F_{z,\text{tot}} = 0$. The driving torque T is given by the circumferential reaction of cam $_1$ applied at radius $r, T = r\left|F_\theta^{\text{cam}1}\right|$. Solving the system of equilibrium equations yields the general and compact expression for the instantaneous required torque Eq. (3).

$$T(\theta) = \frac{rF_{z,\text{tot}}(z,\dot{z})\tan\left(\lambda_1(\psi_1)+\mathrm{sgn}(\dot{z})\phi_1\right)}{1-\frac{\tan\left(\lambda_1(\psi_1)+\mathrm{sgn}(\dot{z})\phi_1\right)}{\tan\left(\lambda_2(\psi_2)+\mathrm{sgn}(\dot{z})\phi_2\right)}} \tag{3}$$

This formula represents the central result of the analysis, valid for T_c (upstroke/loading) and T_s (downstroke/release). A complete cycle of loading is considered, where the mechanism moves from z_0 to $z_{\max}$. The input work during the upstroke is $W_{\text{in,A}} = \int T_c(\theta)d\theta$. The elastic potential energy stored in the spring is $U_s(z_{\max}) = \int F_s(z)dz$. The work dissipated by friction and the damper is $W_{\text{diss,A}} = W_{\text{in,A}} - U_s(z_{\max}) - \int F_{ext}(z)dz$. During the upstroke, the spring returns the stored energy, driving the mechanism back toward z_0. The torque $T_s(\theta)$ can be driving, zero, or resistive (braking), depending on the system conditions. In many cases, the downstroke is driven by the spring force $(F_s(z) + F_{ext}(z))$, and the hydraulic damper is sized to control the velocity. If the actuator is released $(T_c = 0)$, the system reaches a steadystate velocity v_z^* such that the required torque T_s becomes zero, as shown in Eq. (4).

$$F_{z,\text{tot}}(z, v_z^*), \mathrm{sgn}(\dot{z} = -1) = 0 \Longrightarrow F_s(z) + F_{ext}(z) = c|v_z^*| + q(v_z^*)^2 \tag{4}$$

The work exchanged with the actuator is $W_{\text{in,B}} = \int T_s(\theta)d\theta$. If T_s is a braking torque, $W_{\text{in, B}}$ is negative, and $W_{\text{recup}} = -W_{\text{in, B}}$ is the work absorbed by the motor. Efficiency is defined as the ratio of release torque to loading torque at the same position z and specified velocities, as given by Eq. (5):

$$\eta_T(z; v_{\text{load}}, v_{\text{release}}) = \frac{|T_s(z, v_{\text{release}})|}{|T_c(z, v_{\text{load}})|} \tag{5}$$

Using the general expression for torque in Eq. (3) and the definition of efficiency in Eq. (5), the torque efficiency can be written as the ratio between the release and loading torque magnitudes evaluated at the same axial position z, but for opposite motion directions. By explicitly substituting Eq. (3), the efficiency becomes

$$\eta_T(z; v_{\text{load}}, v_{\text{release}}) = \frac{|F_{z,\text{tot}}(z, v_{\text{release}})|}{|F_{z,\text{tot}}(z, v_{\text{load}})|} \left| \frac{\frac{\tan(\lambda_1(\psi_1)-\phi_1)}{1-\frac{\tan(\lambda_1(\psi_1)-\phi_1)}{\tan(\lambda_2(\psi_2)-\phi_2)}}}{\frac{\tan(\lambda_1(\psi_1)+\phi_1)}{1-\frac{\tan(\lambda_1(\psi_1)+\phi_1)}{\tan(\lambda_2(\psi_2)+\phi_2)}}} \right| \quad \text{s} \tag{6}$$

The first factor represents the ratio of total axial forces and therefore includes hydraulic and damping effects through $F_{z,\text{tot}}(z, \dot{z})$. The second factor depends only on the cam geometry (lead angles λ_1, λ_2) and dry friction at the two cam-follower contacts (through ϕ_1, ϕ_2). This form makes the physical trends explicit. The damper (parameters c and q, embedded in $F_{z,\text{tot}}$) reduces the axial driving capability during release, lowering the first factor while ensuring a controlled return. Friction on $cam_1(\phi_1 > 0)$ reduces efficiency through the ratio of the tangent terms; moreover, if $\lambda_1(\psi_1) \leq \phi_1$, the outer cam is self-locking and, within the quasistatic model, the release torque becomes resistive. Friction associated with the inner cam contact ($\phi_2 > 0$) further decreases efficiency through the denominator terms. A value $\eta_T = 0$ corresponds to a non-return condition, for which no braking torque is required ($T_s = 0$).

4. Problem Definition

This section defines the case study used for the efficiency optimisation, analyzing the mechanism under quasi-static conditions over two phases. In the first phase (loading phase), the driven cam rotates while the follower translates and rotates, compressing the spring and storing elastic energy. Initially, the spring is fully uncompressed. As the driven cam rotates, the follower moves, rotating around the cam axes, and the pivot attached to the follower compresses the spring, storing energy, as shown in Fig.2.

In the second phase (release phase), the spring returns the stored energy and drives the follower, generating an output torque through the cam-follower contacts. The torque profile and the associated torque efficiency can be tailored by adjusting the groove inclination (lead angle) of the two cams, along with the spring characteristics and friction conditions. Additionally, it is possible to achieve a specific torque condition by evaluating these factors.

If required, the mechanism can be designed to stop at a prescribed rotation by exploiting the inclination of one cam perpendicular to the spring force vector. The self-locking condition is achieved through an appropriate local groove orientation and cam profile shaping, allowing the mechanism to stop at a specific rotation.

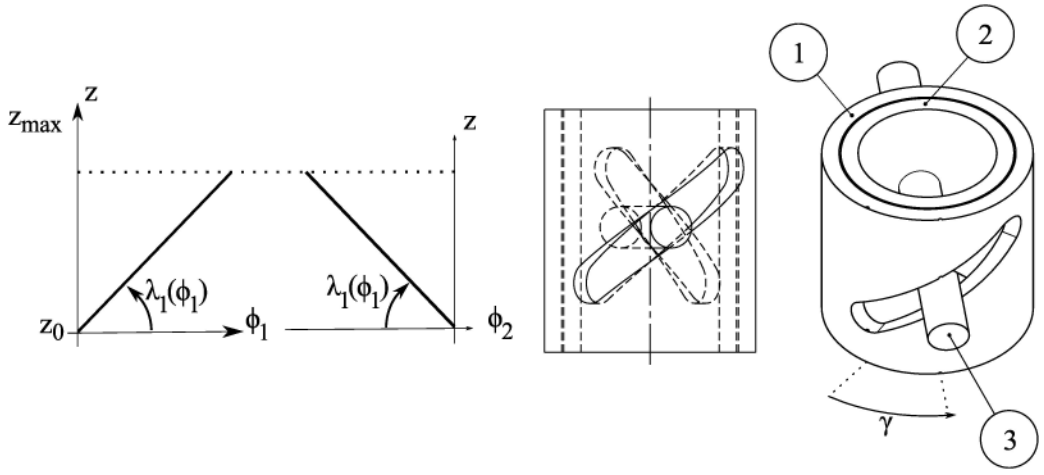

Figure 1: Mechanism Schematic and γ Description. Figure of a Sample of External Cam (1), Internal Cam (2) And the Follower (3). On the left the Unwinded Cams Described in the Reference Frame z/ϕ_i

The released torque can be achieved by properly designing the cam geometry. When unwrapping cylindrical cam profiles, it is important to consider practical manufacturability limits. Specifically, the follower's radius must be smaller than the cam's to ensure proper engagement. Additionally, the manufacturing process must account for the material and the effects of heat-treatment processes such as hardening, which can introduce surface distortions in the cam. Steel tempering, for instance, induces changes in the cam geometry due to thermal expansion and contraction,

potentially altering the profile. This could lead to challenges in achieving the precise dimensions required for small features, especially at the contact point between the cam and the follower. Furthermore, small geometries may not withstand the cyclical stresses involved in the cam's operation, potentially leading to premature wear or failure. Therefore, design tolerances must account for both the effects of manufacturing processes and the mechanical stresses the cam will experience during operation to ensure reliable operation throughout its lifespan.

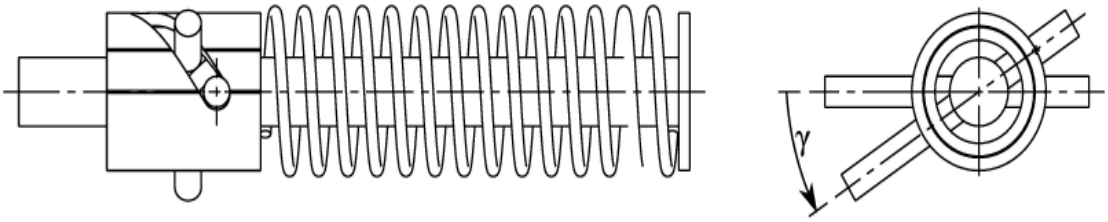

Figure 2: Orthogonal View of the mechanism. Position of the Spring and Follower Motion During Decompression and Compression. Definition of the Angle γ, Measured from the Follower's Starting Position

The theoretical model is simplified by assuming two generic cams made of the same material and a single constant friction factor μ. While this assumption is valid for a first-order analysis, in real operating conditions, both pressure-dependent and velocity-dependent friction effects could influence system performance. Specifically, as pressure increases, the contact area between the cam and the follower increases, which typically leads to a higher frictional force. This can be modelled using a pressure-dependent friction coefficient that follows a form such as the Stribeck curve, in which friction varies with sliding velocity and load pressure. In our case, the velocity variation (from 0 to 0.1 m/s) is relatively small, so velocity-dependent effects are expected to have a minimal impact on efficiency. This effect will be validated experimentally during testing, where real measurements will refine the model. It is possible to see the working configuration (Fig. 1) piece by piece and the assembly settings.

The hypothesis at the base is that cam1 drives the cam two due to the force $F_s(z)$ imposed by the follower and the spring. During the second operating phase, cam_2 is driven by an external torque while cam1 remains fixed, causing the follower to compress the spring. The model Fig.3 and Fig.4 shows the effect of sliding friction. As noted above, the mechanism must absorb energy during the compressing phase and release it during the stretching phase. The equations of static equilibrium on $Z-axis$ and θ gives the values of the internal forces of the system under compressing and stretching conditions. The inclinations of the two $cams$ are evaluated in the point where the follower touches a cam, that is, in the tangent point of the circle that represents the follower. The angle $\lambda_2(\phi_2)$ represents the inclination of cam1 calculated from the positive x axis to the tangent and $\lambda_1(\phi_1)$ is the angle to identify cam two, calculated from the negative $x-axis$ to the tangent between the follower and the second cam. The equilibrium of forces exchanged Eq. (8) between cams and follower gives the possibility of estimating the magnitudes of the forces at play in the mechanism. Identifying the configuration of the friction in the compressing and stretching phase is fundamental for talking about efficiency. One approach to compute the internal forces is to write the force-balance equations and resolve the components along the $z-axis$. To close the system, a moment equilibrium about the $z-axis$ is also required, because the two cams act through different effective lever arms due to their different diameters. The lever is considered as the minimum distance from the $Z-axis$ and the cylinder in the middle of the inner and outer cylinders of every cam.

During the first phase of operation, the spring is compressed, and the friction force acts in the opposite direction to the velocity, resulting in the system described by equation Eq. (8), where (A_1 and A_2 denote the friction terms. The complete model may consider two distinct friction models, one for each cam, to better capture the system's behavior. Since the cams are made of the same material and the contact surfaces are lubricated, a Coulomb-type friction model is adopted in this case. This choice is justified by the very low relative velocity involved (approximately 0.01 m/s), for which viscous effects can be considered negligible. The only constant friction coefficient μ is included in the A_n terms, which are expanded in the subsequent Eq. (10). A single coefficient is adopted since all cams share the same material and operate under mandatory lubrication. When the spring extends, the system enters the second phase, described by equation Eq. (9). In this phase, the friction force reverses direction along with the velocity, and the friction term A_n is expanded as shown in Eq. (11).

$$\begin{cases}\sum F_x = 0\\ \sum F_z = 0\end{cases} \tag{7}$$

$$\begin{cases} A_2\sin(\lambda_1) + R_2\cos(\lambda_1) + R_1\cos(\lambda_2) - A_1\sin(\lambda_2) = F_s \\ \big(A_2\cos(\lambda_1) + R_2\sin(\lambda_1)\big)r_2 - \big(A_1\cos(\lambda_2) + R_1\sin(\lambda_2)\big)r_1 = 0 \end{cases} \tag{8}$$

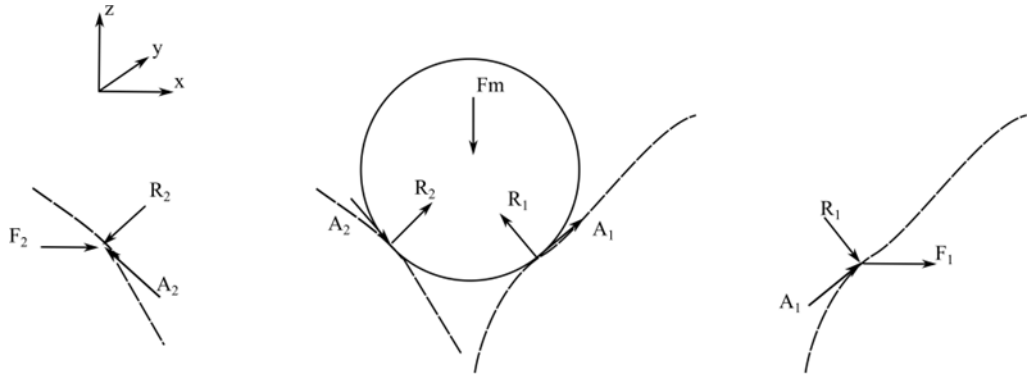

Figure 3: Kinetostatic Model of the Compression Phase. The Two Cams are Unwrapped, with Three Distinct Systems Presented Sequentially: on the Left, The Forces Acting on the First Cam Are Shown; in the Center, The Forces Acting on the Follower Are Depicted; and on the Right, The Forces on the Second Cam Are Illustrated.

$$\begin{cases} A_2\sin(\lambda_1) + R_2\cos(\lambda_1) + R_1\cos(\lambda_2) + A_1\sin(\lambda_2) = F_s(z) \\ \big(A_2\cos(\lambda_1) + R_2\sin(\lambda_1)\big)r_2 - \big(-A_1\cos(\lambda_2) + R_1\sin(\lambda_2)\big)r_1 = 0 \end{cases} \tag{9}$$

$$\begin{cases} (\cos(\lambda_1)\cdot\mu\cdot r_2 + \sin(\lambda_1)\cdot r_2)\cdot R_2 + (-\cos(\lambda_2)\cdot\mu\cdot r_1 = \sin(\lambda_2)\cdot r_1)\cdot R_1 \\ \big(-\sin(\lambda_1)\cdot\mu + \cos(\lambda_1)\big)\cdot R_2 + \big(-\sin(\lambda_2)\cdot\mu + \cos(\lambda_2)\big)\cdot R_1 = F_s \end{cases} \tag{10}$$

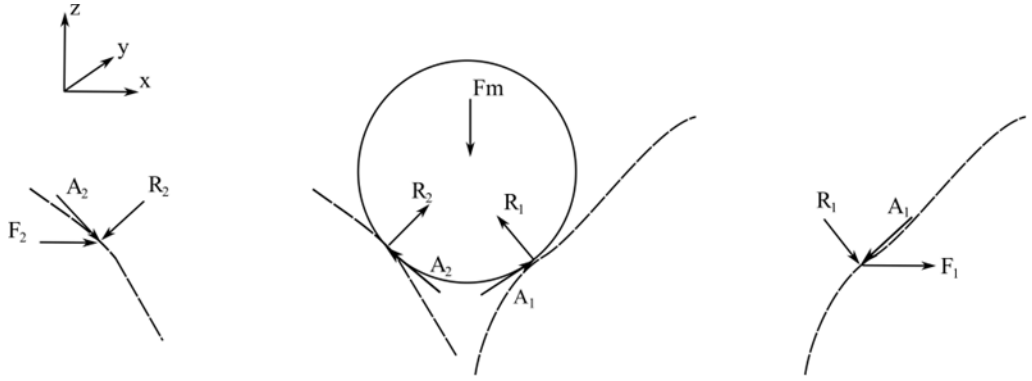

Figure 4: Kinetostatic Model of the Release Phase. The Two Cams are Unwrapped, with Three Distinct Systems Presented Sequentially: on the Left, the Forces Acting on the First Cam Are Shown; in the Center, the Forces Acting on the Follower Are Depicted; and on the Right, The Forces on the Second Cam are Illustrated.

$$\begin{cases} -\cos(\lambda_1)\cdot\mu\cdot r_2 + \sin(\lambda_1)\cdot r_2)\cdot R_2 + (\cos(\lambda_2)\cdot\mu\cdot r_1 = \sin(\lambda_2)\cdot r_1)\cdot R_1 \\ \big(\sin(\lambda_1)\cdot\mu + \cos(\lambda_1)\big)\cdot R_2 + \big(\sin(\lambda_2)\cdot\mu + \cos(\lambda_2)\big)\cdot R_1 = F_s \end{cases} \tag{11}$$

Resolving the systems, it is possible to obtain the values of R1 Eq. (12) and R2 Eq. (13) during the compression phase. For the compactness the term M Eq. (14) and N Eq. (15) are described below. In the stretching phase the expressions obtained are similar as calculated before.

$$R_1 = \frac{F_s r_2(\mu\cos\lambda_1 + \sin\lambda_1)}{r_1 M + r_2 N} \tag{12}$$

$$R_2 = \frac{F_s r_1(\mu\cos\lambda_2 + \sin\lambda_2)}{r_1 M + r_2 N} \tag{13}$$

$$M = (\cos\lambda_1 - \mu\sin\lambda_1)(\mu\cos\lambda_2 + \sin\lambda_2) \tag{14}$$

$$N = (\mu\cos\lambda_1 + \sin\lambda_1)(\cos\lambda_2 - \mu\sin\lambda_2) \tag{15}$$

Taking into account the schematic of the model of the two phases, it is possible to obtain the equation of the torque on cam1 is computed as the normal force multiplied by its effective lever arm, including frictional contribution. Assuming the friction $A1 = \mu R_1$ helps to describe the torque using a unique Eq. (16)-(17). The sign change in the term $\mu\cos(\lambda_2)$ indicates the reversal of the friction direction.

$$T_{\mathrm{c,\,th}} = R_{1\mathrm{c}} \cdot r_1 \cdot \left(\cos(\lambda_2) \cdot \mu + \sin(\lambda_2)\right) \tag{16}$$

$$T_{\mathrm{s,\,th}} = R_{1\mathrm{s}} \cdot r_1 \cdot \left(-\cos(\lambda_2) \cdot \mu + \sin(\lambda_2)\right) \tag{17}$$

$$\eta_T = \frac{T_{\mathrm{s,\,th}}}{T_{\mathrm{c,\,th}}} \tag{18}$$

The velocity of the mechanism is constant and regulated by a nozzle that controls the fluid flow within a channel, where a hydraulic piston is connected to the end of the spring causing the fluid circulation.

One of the objectives of this paper is to optimize the efficiency described as the ratio between $T_{\mathrm{s,\,th}}$ and $T_{\mathrm{c,\,th}}$. The aim is to maximise the function of efficiency Eq. (18) by varying the geometry of the cams assuming a constant factor to describe the friction.

5. Efficiency Analysis

The maximization of the efficiency η_T, which involves multiple trigonometric components, posed a challenge due to the oscillatory nature of sine and cosine terms. A grid-based numerical search was employed. Let $\eta_T(\lambda_1, \lambda_2)$ be a real-valued function where λ_1 and λ_2 appear inside trigonometric functions such as $\sin(\lambda_1)$, $\cos(\lambda_2)$, or combinations thereof. The multi-grid exploration Fig.5 was employed to analyze the function's behavior over the domain λ1, λ2 ∈ [0, π/2] rad. The techniques impose values for λ_1 and λ_2 having a look at the result of the function Eq. (18). The numerical exploration consistently indicated an optimum at λ_1 =π/4 rad and λ_2 =π/4 rad, regardless of μ or applied load.

This study highlights the effectiveness of graphical methods in complementing analytical techniques, particularly when dealing with intricate trigonometric functions. In scenarios where explicit differentiation is cumbersome, numerical and visual strategies provide an efficient alternative to identifying extrema.

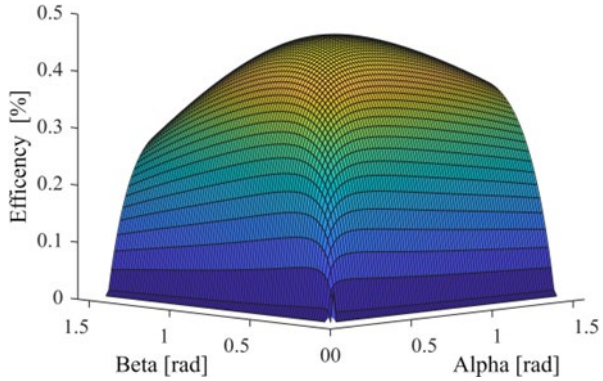

Figure 5: η_T of the Mechanism Evaluating the Inclination λ_1 and λ_2 of the Two Cams

6. Experimental Setup and Model Validation

To validate the predictive capabilities of the proposed model, an experimental campaign was carried out using two physical prototypes of the mechanism described in Section 4. The cam and follower components were manufactured from hardened steels commonly used in high-load mechanical applications. The constant coefficient of friction reflects typical conditions for hardened steel-on-steel interfaces under boundary lubrication. Specifically, a value of μ = 0.14 was adopted for the lubricated interface with $Grease_1$ and $\mu = 0.19$ for $Grease_2$. These values fall within the commonly reported range in the literature for steel-on-steel sliding applications (0.08–0.20), thereby supporting the validity of the model in representing realistic tribological behavior. The samples were tested under controlled laboratory conditions to evaluate torque behavior. Two different lubricants, here referred to as $Grease_1$ and $Grease_2$, were used to assess the influence of friction on torque performance. $Grease_1$, featuring a PTFE thickener and MoS additives, with a high-base oil viscosity of 1400 cSt at 40°C and 150 cSt at 100°C, provided excellent load resistance

and smooth motion under pressure. $Grease_2$, a lithium-complex grease enhanced with boron-derived additives, offered a base oil viscosity of 1000 cSt at 40°C, exceptional thermal stability up to 180°C and effective reduction of stick-slip phenomena, making it ideal for high-load sliding applications.

6.1 Test Bench and Measurement Procedure

A dedicated test bench was designed and assembled to measure the torque generated by the mechanism. The core of the setup consists of a rigid support structure used to constrain the cam hinge, while a steel lever arm of length L = 0.500 m was rigidly attached to the rotating cam_2 (inner cam). The torque was indirectly measured by applying a force at the end of the lever arm and recording the reaction using a digital force gauge sliding on a sled. The setup enables planar measurement of the torque.

The force measurements were performed using a SAUTER FK 50 digital dynamometer with a measurement range from 0 to 50 N and a resolution of 0.02 N. The instrument provides an accuracy of ±0.1% of full scale and operates at a sampling rate of 1,000 Hz. The dynamometer is equipped with overload protection up to 120% of its maximum capacity and includes a peak-hold function for the capture of transient force values.

The measurement procedure consisted of manually rotating the cam until the desired angular position was reached. The force applied at the end of the lever was measured at equilibrium using the dynamometer and the torque was then computed using the relationship $T_{th} = F.L$, where F is the measured force and L = 0.500 m is the lever length. The effective lever length was set by machining a hole at the specified distance. The procedure was repeated in small angular increments (typically every 0.08727 rad and 0.01745 rad near 0 rad and 1.3963 rad) over the full operating range of the mechanism. Each measurement was repeated three times to reduce random errors and the average value was taken as the final result. The total uncertainty in the torque measurement arises from the uncertainty in the force reading, the uncertainty in the lever-arm length, and a possible misalignment between the applied force and the lever arm. Since torque is computed from the measured force and lever length, the combined relative uncertainty $\delta T/T$ is evaluated according to Eq. (19):

$$\frac{\delta T}{T} = \sqrt{\left(\frac{\delta F}{F}\right)^2 + \left(\frac{\delta L}{L}\right)^2 + \left(\frac{\sin\,\delta\theta}{\sin\theta}\right)^2}. \tag{19}$$

In Eq. (19), the force uncertainty is $\delta F = 0.05\,N$, derived from the dynamometer accuracy (0.1% of full scale), the lever-arm uncertainty is $\delta L = 1 \times 10 - 4\,m$, corresponding to a manual measurement tolerance of 0.1 mm, and $\delta\theta = 0.05236$ rad represents the possible deviation from the nominal perpendicular configuration $\theta = \pi/2$, caused by a 10 mm error over the 200 mm height of the dynamometer arc.

For a representative operating condition with $F = 20.00\,N$, corresponding to a torque $T = 10.00\,Nm$, the individual relative uncertainty terms are evaluated as shown in Eq. (20).

$$\frac{\delta F}{F} = 0.0025, \frac{\delta L}{L} = 2 \times 10^{-4}, \frac{\sin\,\delta\theta}{\sin\theta} = 0.05234. \tag{0(20)}$$

Substituting these values into Eq. (19), the absolute torque uncertainty is obtained as:

$$\delta T = 10.00\sqrt{(0.0025)^2 + (2 \times 10^{-4})^2 + (0.05234)^2} = 0.524\text{Nm}. \tag{21}$$

Equation (21) corresponds to a relative uncertainty of approximately 5.24%, which is considered acceptable for model validation purposes, particularly when the analysis focuses on trend comparison rather than absolute accuracy. All measurements were performed at a controlled ambient temperature of 18 ±2 °C.

6.2 Torque Curves and Model Comparison

Fig.6 shows the torque measured experimentally for each type of grease, compared with the theoretical predictions obtained from the model. As expected, the measurements using $Grease_2$, which has lower viscosity, are closer to the predicted trend.

6.3 Internal Reactions Estimation

In addition to torque validation, the internal reaction forces acting on the follower were estimated using the model equations and compared with experimental observations. These reactions play a critical role in the wear, stability and long-term performance of the mechanism.

Fig.7 illustrates the estimated internal reaction forces as a function of the cam angle, providing valuable insights into the design implications for load distribution and material selection. This information can be used to further refine the geometry of the follower and cam surfaces to minimize stress concentrations and improve mechanical robustness.

The results confirm the effectiveness of the model, particularly in low-friction conditions and support the theoretical conclusion that an inclination

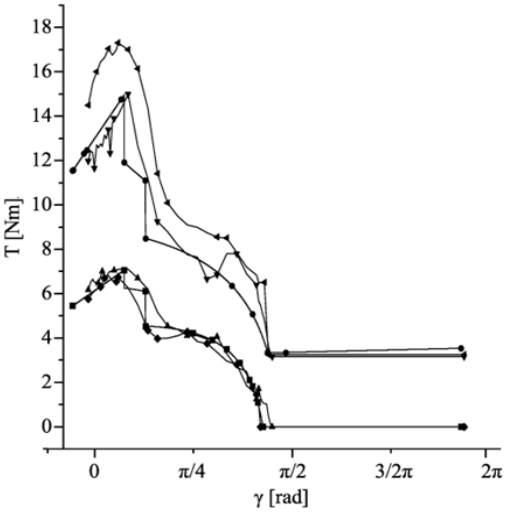

Figure 6: Measured and Predicted Torque Curve (Nm/Rad) Using Different Grease vs the Rotation γ [rad]. Up Triangle, Lower Triangle, Right Triangle, Diamond, Square and Circle Represent, Respectively, Stretch Measured $Grease_2$, Compress Measure $Grease_1$, Compress Measured $Grease_2$, Stretch Measured $Grease_1$, Stretch Theoretical, Compress Theoretical.

of π/4 rad for both cams maximizes the system efficiency η_T. The validation also demonstrates the practical viability of the design under realistic operating conditions.

7. Case Studies on Cam Designs

After validating and tuning the proposed model, this section applies the framework to two specifically designed pairs of cylindrical cams. The aim is to evaluate how accurately the torque forecast from the analytical model matches the experimental measurements.

The same test bench and methodology described in Section (7) were used. Each cam pair was fabricated according to the optimized design criteria, ensuring concentricity and controlled lubrication. For both designs, the torque angle response was measured during compression and stretching phases. Solution A uses a cam_2 (inner cam) with a starting inclination of 0.8203 rad

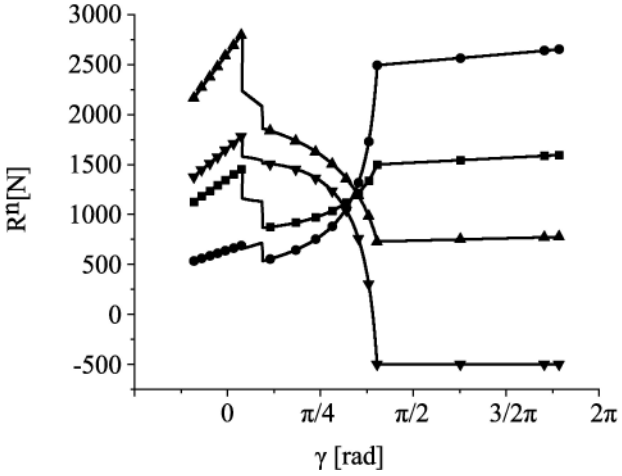

Figure 7: Estimated Internal Reactions [N] vs the Rotation θ [rad] Between Cams, Acting on the follower During Operation. Up Triangle, Lower Triangle, Square and Circle Represent, Respectively, cam_1 Compression, cam_1 Stretching, cam_2 Compression and cam_2 Stretching.

and a cam_1 (outer cam) with a smaller radius. cam2 of the solution B starts at 0.8552 rad and is paired with cam1 that has a larger elliptical arc.

7.1 Results for Cam Pair A

Fig.8 shows the comparison between the predicted torque curve and the experimental measurements for the first cam pair. The agreement is generally strong, with only minor deviations observed near the transition points, likely due to hysteresis introduced by friction reversal. The efficiency peak matches the theoretical forecast within an RMSE of 0.735 Nm in the decompression phase and 0.451 Nm in the compression.

7.2 Results for Cam Pair B

While the overall trend remains consistent with the model, the force components that generate torque become more influential in this configuration, and the constant-friction assumption is less accurate. Tribological effects are not fully captured, particularly under higher contact pressures. In this case, the internal reactions increase by approximately 40%, which amplifies frictional effects and leads to a different response than predicted by the kinetostatic model. The RMSE is 0.69 Nm for the decompression phase and 1.51 Nm for the compression phase.

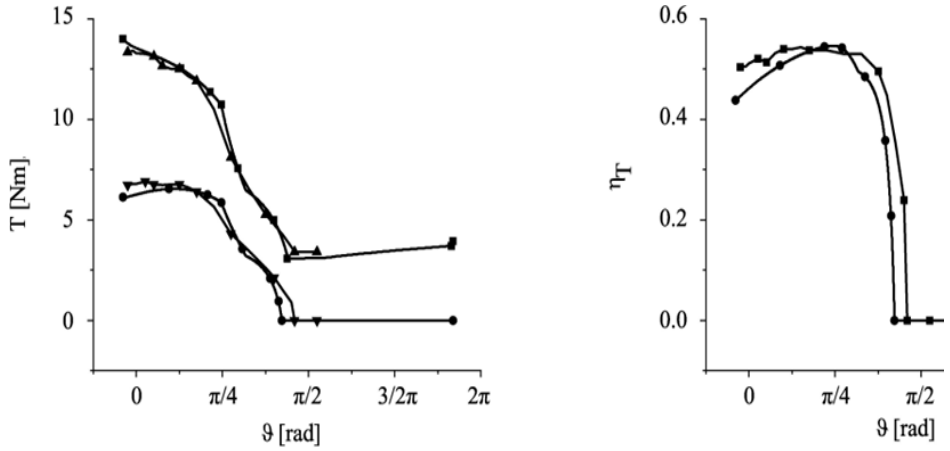

Figure 8: Left Side, the Predicted and Measured Torque [Nm] vs the Rotation θ [rad] for Cam Pair A. Up Triangle, Lower Triangle, Square and Circle Represent, Respectively, $T_{s,m}$, $T_{c,m}$, $T_{c,th}$ and $T_{s,th}$. Right Side, the Efficiency η_T vs the Rotation θ [rad]. Square and Circle Represent, Respectively, Theoretical Efficiency and Measured.

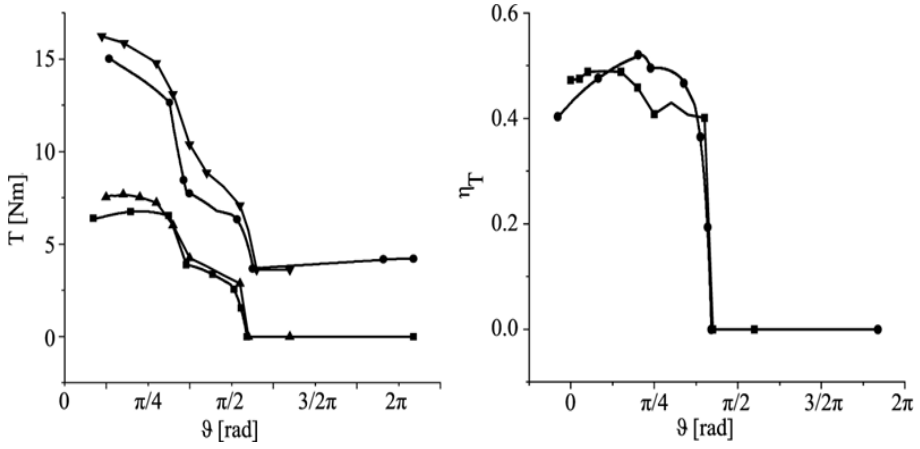

Figure 9: Left Side, the Predicted and Measured Torque [Nm] vs the Rotation θ [rad] for Cam Pair B. Up Triangle, Lower Triangle, Square and Circle Represent, Respectively, $T_{c,m}$, $T_{s,m}$, $T_{s,th}$ and $T_{c,th}$. Right Side, the Efficiency η_T vs the Rotation θ [rad]. Square and Circle Represent, Respectively, Theoretical Efficiency and Measured.

8. Discussion

The comparison between predicted and experimental torque curves for both cam pairs confirms that the proposed

model accurately captures the principal mechanical behavior of the novel cylindrical cam mechanism. Particularly, the model's predictive reliability under low-friction conditions, such as those achieved using $Grease_2$, demonstrates its effectiveness in guiding practical design. As mentioned in the article all tests were at a constant speed.

Some deviations were observed between the measured and theoretical torque, particularly for cam pair B. The root causes of these deviations include friction hysteresis during the transition between the compression and decompression phases, simplified friction modeling that assumes a constant coefficient and does not account for pressure-dependent tribological behavior, geometric imperfections arising during cam manufacturing despite efforts to maintain concentricity and optimized surface finish, and the friction effect. The latter was found to increase internal forces by nearly 40%, potentially shifting the dominant contact behavior and raising the risk of surface pitting, micro-fatigue, and inaccurate predictions.

Despite these limitations, the deviations remained within acceptable engineering tolerance. The root mean square error (RMSE) values were all below 1.5 Nm in the compression phase and below 0.7 Nm on decompression and within the 5% uncertainty range estimated in the experimental setup. This validates the model's reliability and reinforces the conclusion that a cam inclination angle of π/4 rad for both cams yields optimal efficiency.

The graphical optimisation approach, adopted due to the high complexity of the analytical derivatives of the efficiency function η_T, proved to be both robust and practical. For scenarios involving intricate trigonometric functions where symbolic methods become computationally infeasible, such numerical techniques provide valuable insights into parameter tuning.

From an engineering perspective, the efficiency model provides a powerful tool for optimizing compact, spring-loaded cam mechanisms designed for controlled torque delivery. The dual-cam configuration enables precise control of energy storage and release, offering significant advantages over traditional single-cam systems, particularly in applications that require a compact, robust design, high torque repeatability, and resistance to load variations, such as robotics, prosthetics, and automotive actuation systems.

However, it is important to note that the model's current limitations arise from its assumption of constant friction. The observed 40% increase in internal reaction forces for cam pair B highlights the need for improved tribological models that account for velocity-dependent friction coefficients, lubrication behavior under varying pressure and temperature, and the effects of surface roughness and wear over time.

Future extensions of this work may include developing a dynamic model that incorporates inertial effects, as well as fatigue analysis of the cams and follower. The friction model could be improved by adding additional terms rather than a constant factor. For example, the Archard wear equation, V = KFs H, relates wear volume V to the normal load F, sliding distance s, material hardness H and a dimensionless wear coefficient K, characterizing material loss under sliding contact.

9. Conclusions

This study presents a novel cylindrical cam mechanism capable of storing and releasing energy through a spring-based interaction between two concentric cams and a follower. A detailed static and kinetostatic model was developed and analytical equations were derived to describe the internal forces and torque generated during both compression and stretching phases. The proposed mechanism achieved maximum efficiency at a cam inclination angle of π/4 rad, a result confirmed through graphical optimisation and experimental validation. The experimental setup, using various lubricants and precision measurements, demonstrated strong alignment with theoretical pre dictions, confirming the model's reliability under realistic conditions. These findings support the mechanism's application in systems requiring compact, energy-efficient torque generation. Future work may include the incorporation of dynamic modeling, fatigue analysis and control strategies for adaptive performance in real-world mechanical environments.

10. Nomenclature

All symbols below are defined as used in the theoretical development. SI units or dimensions are indicated in square brackets.

R_1, R_2	Normal reaction forces at cam1 and cam2 [N]
M, N	Terms to synthesize the denominator of R1 and R2 [–]
A_1, A_2	Friction forces at cam–follower interfaces [N]; Ai = μRi
μ	Coefficient of sliding friction [–]
θ	Rotation of the external load [rad]
ϕ_i	Friction angle at cami-follower contact [rad]
λ_i	Generic helix function that describe a specific inclination at ϕ_i [rad]

r_1, r_2	Effective cam radii (lever arms) [m]
$\lambda_1(\phi_1), \lambda_2(\phi_2)$	Cam profile inclination angles [rad]
γ	Angle of axial rotation of the follower [rad]
ψ_i	Angular position of cam_i in the relative reference frame [rad]
z	Axial displacement of the follower [m]
ζ	Dummy integration variable (axial displacement) [m]
$\dot{z}$	Axial velocity of the follower [ms^{-1}]
$F_s(z), k, F_0$	Spring force on follower [N]; stiffness k [Nm^{-1}]; preload $F_0[N]$
$D_v(z, \dot{z})$	Damper (damping) force on follower [N]
c	Laminar (linear/viscous) damping coefficient [Nsm^{-1}]
q	Turbulent (quadratic) damping coefficient [Ns^2 m^{-2}]
$T_{\mathrm{c,th}}$	Theoretical torque during spring compression [Nm]
$T_{\mathrm{s,th}}$	Theoretical torque during spring stretching [Nm]
$T_{\mathrm{c,m}}$	Measured torque during spring compression [Nm]
$T_{\mathrm{s,m}}$	Measured torque during spring stretching [Nm]
η_T	Torque efficiency, $\eta_T = T_{\mathrm{stretch}}/T_{\mathrm{compress}}[-]$
HRC	Rockwell Hardness, Scale C (dimensionless index). Test load 150kgf = 1470.9975N

Note: cam1 refers to the outer cam (fixed) and cam2 the inner cam (rotating) in this study's context. It is assumed that the follower has a circular cross-section (roller), so the cam profile's "inclination angle" is measured relative to the follower's centre. Views are represented according to ISO standard

References

Alakhramsing, S. S., de Rooij, M., Schipper, D. J., & van Drogen, M. (2018). Lubrication and frictional analysis of cam–roller follower mechanisms. *Proceedings of the Institution of Mechanical Engineers, Part J: Journal of Engineering Tribology*, *232*(3), 347-363. https://doi.org/10.1177/1350650117718083

Alamsyah, C., Dillich, S., & Pettit, A. (1989). Effects of initial surface finish on cam wear. *Wear*, *134*(1), 29-47. https://doi.org/10.1016/0043-1648(89)90060-4

Angeles, J., & López-Cajún, C. S. (2012). *Optimization of cam mechanisms* (Vol. 9). Springer Science & Business Media. https://doi.org/10.1007/978-94-011-3572-6

Aversa, R., Petrescu, R. V., Akash, B., Bucinell, R., Apicella, A., & Petrescu, F. I. (2017). Cam-gears forces, velocities, powers and efficiency. *American Journal of Engineering and Applied Sciences*, *10*(2), 491-505. https://doi.org/10.3844/ajeassp.2017.491.505

Baş, H. (2021). Investigation of effects of surface roughness on the performance of cam mechanisms. *International Journal of Automotive Engineering and Technologies*, *10*(1), 67-73. https://doi.org/10.18245/ijaet.843229

Cardoso, D. S., Fael, P. O., Gaspar, P. D., & Espírito-Santo, A. (2025). Balancing cam mechanism for instantaneous torque and velocity stabilization in internal combustion engines: Simulation and experimental validation. *Energies*, *18*(13), 3256. https://doi.org/10.3390/en18133256

Català, P., Antònia De los Santos, M., Veciana, J. M., & Cardona, S. (2016). Avoiding early failures in conjugate cam mechanism by means of different design strategies. *Journal of mechanical design*, *138*(1), 012302. https://doi.org/10.1115/1.4031805

Cerit, A. A., Nair, F., Zafar, H. M., & Karamış, M. (2023). Comparison of the surface morphologies of ceramic reinforced metal matrix composite cams after wear tests under dry and wet conditions. *Journal of Composite Materials*, *57*(9), 1541-1556. https://doi.org/10.1177/00219983231159720

Demeulenaere, B., & De Schutter, J. (2005). Input torque balancing using an inverted cam mechanism. *Journal of mechanical design*, *127*(5), 887-900. https://doi.org/10.1115/1.1876452

Gao, F., Liu, Y., & Liao, W.-H. (2018). Cam profile generation for cam-spring mechanism with desired torque. *Journal of Mechanisms and Robotics*, *10*(4), 041009. https://doi.org/10.1115/1.4040270

Hren, I., Hejma, P., Michna, Š., Svoboda, M., & Soukup, J. (2018). Analysis of torque cam mechanism. In *MATEC Web of Conferences* (Vol. 157, pp. 06004). EDP Sciences. https://doi.org/10.1051/matecconf/201815706004

Kim, J., Moon, J., Kim, J., & Lee, G. (2020). Compact variable gravity compensation mechanism with a geometrically optimized lever for maximizing variable ratio of torque generation. *IEEE/ASME Transactions on Mechatronics*, *25*(4), 2019-2026. https://doi.org/10.1109/TMECH.2020.2998291

Kolozsvary, Z. (1973). The study of surface fatigue in sliding wear. *Wear*, *25*(2), 215-224. https://doi.org/10.1016/0043-1648(73)90073-2

Mundo, D., Liu, J.-Y., & Yan, H.-S. (2006). Optimal synthesis of cam-linkage mechanisms for precise path generation. *Journal of mechanical design*, *128*(6), 1253-1260. https://doi.org/10.1115/1.2337317

Sun, Y., Tang, P., Zheng, J., Dong, D., Chen, X., Bai, L., & Ge, W. (2019). Optimal design of a nonlinear series elastic actuator for the prosthetic knee joint based on the conjugate cylindrical cam. *IEEE Access*, *7*, 140846-140859. https://doi.org/10.1109/ACCESS.2019.2944206

Tsay, D. M., Ho, H. C., & Wang, K. C. (2002). Design of torque balancing cams for globoidal cam indexing mechanisms. *J. Mech. Des.*, *124*(3), 441-447. https://doi.org/10.1115/1.1479690